

High thermoelectric performance of environmentally friendly sodium-doped $\text{Cu}_2\text{ZnSnS}_4$ single crystal: Evidence of valleytronics based strategy

Akira Nagaoka (✉ nagaoka.akira.m0@cc.miyazaki-u.ac.jp)

University of Miyazaki

Kenji Yoshino

University of Miyazaki

Taizo Masuda

Toyota Motor Corporation (Japan)

Taylor Sparks

University of Utah <https://orcid.org/0000-0001-8020-7711>

Michael Scarpulla

University of Utah

Kensuke Nishioka

University of Miyazaki

Article

Keywords:

Posted Date: August 11th, 2020

DOI: <https://doi.org/10.21203/rs.3.rs-50170/v1>

License:  This work is licensed under a Creative Commons Attribution 4.0 International License.

[Read Full License](#)

High thermoelectric performance of environmentally friendly sodium-doped $\text{Cu}_2\text{ZnSnS}_4$ single crystal: Evidence of valleytronics based strategy.

Akira Nagaoka^{1*}, Kenji Yoshino², Taizo Masuda³, Taylor D. Sparks⁴, Michael A. Scarpulla⁴, and Kensuke Nishioka¹

¹Research Center for Sustainable Energy & Environmental Engineering, University of Miyazaki, Miyazaki 889-2192, Japan

²Department of Applied Physics and Electronic Engineering, University of Miyazaki, Miyazaki 889-2192, Japan

³S-Frontier Division, Toyota Motor Corporation, Shizuoka 411-0019, Japan

⁴Department of Materials Science and Engineering, University of Utah, Salt Lake City, Utah, 84112 USA

*Corresponding author: akira.nagaoka.m0@cc.miyazaki-u.ac.jp

Thermoelectrics (TEs) are an important class of technologies for harvesting electric power directly from heat sources. To design high performance TE materials, valleytronics has great theoretical potential to maximize a dimensionless figure of merit ZT but has not yet been demonstrated experimentally. Pseudocubic structure approach based on valleytronics paves a new path to manipulate valley degeneracy and anisotropy with low thermal conductivity caused by short-range lattice distortion. Here, we report a record high $ZT = 1.6$ around 800 K, realized in totally environmentally benign Na-doped $\text{Cu}_2\text{ZnSnS}_4$ (CZTS) single crystal. The exceptional performance comes from a high power factor while maintaining intrinsically low thermal conductivity. The results demonstrate that valleytronics is a new strategy and direction in the TE field, which takes advantage of simple material nature tuning without complex techniques.

Many different strategies for improving the dimensionless figure of merit $ZT = S^2\sigma T/\kappa$, where S is the Seebeck coefficient, σ is the electrical conductivity, T is temperature, and κ is the thermal conductivity, have been conducted for thermoelectric (TE) application. These concepts include, but are not limited to, phonon-glass electron-crystal¹ or phonon-liquid electron-crystal², nanostructure modification by alloying and doping to reduce thermal conductivity or to enhance electrical properties by doping and alloying techniques³⁻⁸, improvement of Seebeck coefficient by electronic density of states (DOS) distortion⁹, the conduction (valence) band tuning¹⁰, quantum confinement effects¹¹, and electron energy barrier filtering¹². Low thermal conductivity is possible by inducing nanostructure^{13, 14} and hierarchical architecture^{15, 16}. So far, the $ZT = 2.6$ for SnSe¹⁷ has been achieved by anisotropic properties^{18, 19}, multiple valence bands^{20, 21}, and three dimensional charge and two dimensional phonon transport²². Nevertheless, for large-scale deployment of TE devices, TE materials will have to simultaneously fulfill tough requirements such as non-toxicity, non-scarcity and high efficiency. However, totally environmentally friendly TE materials by current strategies demonstrate far lower ZT values than TE state-of-the-art such as 1.1 for SnS²³.

An unexplored approach for TE optimization is the emerging field of valleytronics. Valleytronics relies on the manipulation of the electronic band structure valley degree of freedom for functional materials to accomplish application needs. This idea was initially applied to new quantum computation devices to carry and store information²⁴. We unify traditional TE approaches into valley factors: the number of valleys contributing to electronic transport (valley degeneracy), the distortion of DOS (valley distortion), and the exact shape of valleys which can be expressed as the effective mass of carriers (valley anisotropy).

Pseudo-cubic approach of multinary compounds paves a path to manipulate the electronic band structure²⁵. The tetragonal I-III-VI₂ group chalcopyrite structure is analogous to a 1×1×2 supercell expansion of the zinc-blende structure. It is easy for non-cubic structure to understand low symmetry with crystal-field splitting Δ_{CF} which leads to low valley degeneracy. This approach is that Δ_{CF} could be tuned to 0 when the crystal structure parameter η is equal to 1 ($\eta = c/2a$, where c and a are lattice parameters for chalcopyrite), which means pseudo-cubic structure. This long-range cubic-like structure regains the valley degeneracy and maintains the localized short-range non-cubic lattice distortions.

Here, this novel pseudo-cubic approach based on valleytronics is applied to achieve a high ZT , environmentally friendly TE material. Single crystals are necessary for optimization of valley parameters, especially valley anisotropy. Typical TE materials have been polycrystalline because grain boundaries scatter phonons disproportionately more than they scatter electrons. This leads to a greater reduction in thermal conductivity than in electrical conductivity and therefore an overall increase in ZT in the last few decades. A pseudo-cubic approach allows the ability to simultaneously optimize electrical and thermal transport properties by long- and short-range structure regions. We focus on the quaternary I₂-II-IV-VI₄ group compound p-type Cu₂ZnSnS₄ (CZTS), which has attracted much attention, mainly in the field of photovoltaic (PV) application. The crystal structure of CZTS is kesterite, closely related to chalcopyrites. Our previous study reveals that η value of CZTS is close to 1 from neutron diffraction measurement, which is ideally suited for a pseudo-cubic approach²⁶. High-quality large-size CZTS single crystals can be obtained to perform experimental thermoelectric measurements on bulk samples²⁷.

Electronic band structure of CZTS

Figure 1a shows the kesterite structure of CZTS, wherein the cation layers of Cu-Sn, Cu-Zn, Cu-Sn and Cu-Zn are alternated along the c -axis. In the Cu-Zn layer, the two atoms are easily disordered leading to short-range distortion for low thermal conductivity. The experimental crystal structure parameter η value of CZTS is 0.997 ($a = 5.455 \text{ \AA}$ and $c = 10.880 \text{ \AA}$), which minimizes the energy splitting parameter ΔCF . The utilization of a rational pseudo-cubic structure supports cubic-like degenerate electronic bands to be high power factor (PF) in Fig. 1b. The electronic band structure of CZTS was computed by density functional theory (DFT) and is shown in Fig. 1c. The spin-orbit interaction is included. Cubic-like valence band edges are observed as a result of the symmetry framework, which is highly degenerate at Γ point indicating an ideal character of pseudo-cubic structure. The band structure with direct bandgap can be observed. As is often the case, the DFT band gap is slightly smaller than the experimental value which we measured to be 1.6 eV for CZTS single crystal by using transient reflectivity measurements²⁸. The top of the valence band is split by the crystal field in Fig. 1d. Kesterite CZTS have Γ_{7+8} symmetry for the topmost (v_1) and second (v_2) valence bands and Γ_{5+6} symmetry for the third band (v_3) where the single state is above the twofold degenerate state with $\Delta CF = 0.06 \text{ eV}$ in the vicinity of Γ point. This theoretical result is in good agreement with a pseudo-cubic approach²⁶. Table 1 shows the anisotropic effective hole masses obtained directly from the band energy dispersion.

TE properties

In this study, we fabricated samples with different compositions including a stoichiometric $\text{Cu}_2\text{ZnSnS}_4$ (**sample 1**), Cu-poor $\text{Cu}_{1.9}\text{ZnSnS}_4$ (**sample 2**), Cu-poor $\text{Cu}_{1.9}\text{ZnSnS}_4$ with Na: 0.1 mol% doped (**sample 3**), and 0.04 mol% doped (**sample 4**) by Sn-solvent traveling heater method

(THM)²⁶. Sodium is known to benefit CZTS PV devices as an effective dopant for enhancement of electrical properties²⁹. Single crystals were cut in the transverse (\perp ; perpendicular to the c -axis) and the longitudinal (\parallel ; parallel to the c -axis) directions for thermoelectric measurements. The structural and compositional properties were investigated by powder X-ray diffraction (XRD), Raman spectroscopy, energy dispersive X-ray spectroscopy (EDX), and inductively coupled plasma atomic emission spectroscopy (ICP-AES) in Supplementary Fig. 1 and Supplementary Tables 1-2.

The temperature dependent electrical and TE properties of CZTS single crystals from 300 K to 800 K are shown in Fig. 2 with the accuracy of TE measurements discussed in Supplementary Figs. 2-4. Consistent with our previous work on CZTS in PV devices, the electrical conductivity with a Cu-poor composition and Na-doping increased by approximately two orders of magnitude greater than the stoichiometric sample (Fig. 2a). We have reported that the carrier transport mechanism can be expressed by band conduction from valence band to defect level near room temperature²⁹. The conductivity data can be described quantitatively as typical thermal activation $\sigma(T) = \sigma_B \exp\left(\frac{-E_A}{k_b T}\right)$, where σ_B is pre-factor, E_A is the relevant activation energy associated with band conduction, and k_b is the Boltzmann constant. The conduction parameters are shown in Supplementary Table 3. The Fermi level lies around the top of the valence band because of typical thermal activation. Therefore, anisotropy of topmost v_1 is dominant for electrical properties. The longitudinal $m_{v_1}^{\parallel}$ is smaller than the transverse $m_{v_1}^{\perp}$, which leads that conductivity along c -axis is higher than that along a -axis. First-principle calculations predict that the dominant shallow V_{Cu} acceptor level under Cu-poor condition is at 20 meV above valence band maximum³⁰. Cu on Zn antisite defect (Cu_{Zn}) becomes a dominant deep acceptor defect at 120 meV under near-stoichiometric and Cu-rich compositions³⁰. The lower E_A in Cu-poor compositions leads to higher

electrical conductivity values because of the increasing concentration of V_{Cu} acceptor. In addition, Na-doping results in the improvement of compensation by suppression of dominant Zn on Cu antisite donor defect (Zn_{Cu})²⁹. This donor defect may be inhibited by a finite Na substitution as neutral Na_{Cu} defect, which is in good agreement with the lowest calculated formation energy of Na_{Cu} by theoretical study³¹. Therefore, the hole mobility and concentration can be enhanced by Na-doping simultaneously in Supplementary Table 3. The scattering process is discussed from temperature dependence of hole mobility in Supplementary Fig. 5.

The sign of the Seebeck coefficient, S , is always positive for all samples as expected for these p-type materials. The values of S monotonically increase with increasing temperature because more holes are thermally activated to high energy states which leads to a higher average entropy of holes originated from valley degeneracy in Fig. 2b. Note that S along a -axis is 10-20% higher than that of c -axis due to heavy effective hole mass from valley anisotropy. Lower S values are observed in Cu-poor compositions and with increasing Na-doping because of the enhanced hole concentration in Table 1. So far, the reported S values of stoichiometric CZTS bulk polycrystalline samples without doping range from 260 to 990 $\mu V/K$ depending on hole concentration near 700 K³²⁻³⁴. The temperature dependence of PF is shown in Fig. 2c. The PF value of **sample 3** along a -axis at 800 K is $1.86 \times 10^{-3} \text{ W/mK}^2$, which is higher than $1.2 \times 10^{-3} \text{ W/mK}^2$ of the state-of-the-art compound Cu_2Se with $ZT = 2.6$ at 850 K³. Our result reveals that high S and σ originated by valley degeneracy and anisotropy leads to high PF value as totally environmentally TE material.

The temperature dependence of thermal conductivity, κ , is shown in Fig. 2d, which was calculated by the thermal diffusivity, λ , specific heat capacity, C_p , and density D . The thermal diffusivity and specific heat capacity dependence on temperature are shown in Supplementary Figs.

3b-3c. Weak anisotropy of thermal conductivity was observed which κ_{\perp} indicates ~3% larger than κ_{\parallel} . The lattice thermal conductivity along a -axis is ~5% larger than that of c -axis in the kesterite structure from theoretical calculation based on the phonon Boltzmann transport³⁵. Weak anisotropy of thermal conductivity in this study is in good agreement with theoretical study³⁵. The thermal conductivity decreases with increasing temperature roughly according to a T^{-1} relation for all samples. This temperature dependence suggests that the lattice thermal conductivity is primarily driven by phonon-phonon Umklapp scattering rather than intrinsic defects. If phonon scattering were driven by neutral dopant-induced, anti-site disorder, or alloy scattering then the scattering would be more uniform over the temperature range with very weak temperature dependence. Such thermal conductivity temperature dependence is typically observed in heavily defected materials such as yttria-stabilized zirconia³⁶. However, here the T^{-1} temperature dependence characteristic of phonon-phonon scattering occurs when other mechanisms like neutral defect scattering are less important. In fact, literature examples exist where the thermal conductivity trend transitions from T^{-1} to nearly temperature independent due to anti-site disorder or mixtures of point defects with Umklapp scattering^{37,38}. In this work, we see evidence that lattice scattering is impacted by the intrinsic complexity of the crystallographic structure. For example, consider the disorder between Cu and Zn by off-stoichiometric compositions and Na-doping. Even though these are single crystals which do not benefit from lattice thermal conductivity reduction due to grain boundary scattering, the values of κ at 800 K are only between 0.94 to 1.7 W/mK. Such low values are only moderately higher than the other reported values of related polycrystalline quaternary compounds such as CZTSe and $\text{Cu}_2\text{CdSnSe}_4$ ^{39,40}. The ability to achieve such low thermal conductivity due to the intrinsic defects in this material while maintaining good electrical transport is an unexpected improvement which can be attributed to the single crystal

nature of these samples. Grain boundaries are typically known to present energy barriers of order 50-150 meV in polycrystalline chalcogenide semiconductors like CZTS⁴¹. Recent literature points out that continued ZT enhancement due to lattice thermal conductivity reduction is fundamentally limited without a means whereby the PF is also enhanced⁴². In light of this, the single crystal approach with a site-disordered material is promising.

Taken together, the outstanding electrical properties with relatively low thermal conductivity of **sample 3** resulted an totally environmentally friendly TE material with TE figure of merit of up to $ZT = 1.6$ at 800 K (Fig. 3). This value is comparable to the highest ZT reported for other relating quaternary materials in Supplementary Table 5. The combined uncertainty of all measurements involved in the calculation of ZT leads to an estimated uncertainty near 30%. Our approach reveals that TE valleytronics concept is comparable with phonon-liquid electron-crystal concept discovering non-toxic earth-abundant Cu_{2-x}S with $ZT = 1.7$ at 1000 K⁴³.

Intrinsic cation fluctuation for low thermal conductivity

Intrinsically disordered structures, such as CZTS where the Cu and Zn cations can exchange site occupancy with little energy cost, lead to low thermal conductivity. Single crystals provide an exceptional opportunity to control and quantify the degree of this fluctuation by simply controlling single crystal cooling rates. The cation fluctuation in CZTS was studied by scanning transmission microscopy (STEM) and EDX relating to structure and chemical composition. Fig. 4a shows a STEM-based image that was subsequently chemically mapped using EDX with the point-resolved Cu-K, Zn-K, Sn-L, and S-K emission lines at micrometer scale. At low magnifications of $\times 11000$ corresponding to the micrometer scale the composition ratio was in good agreement with the expected stoichiometry **sample 1** (Cu:Zn:Sn:S = 24.6:13.0:12.2:50.2). Considering the

correlations in elemental composition, we computed and compiled the Cu/Zn, Cu/Sn, and Zn/Sn maps to discuss the compositional fluctuation at the 50 nm scale length in Fig. 4b. These cation fluctuations, which are effective for phonon scattering, were observed at high magnification in all CZTS single crystals grown by gentle cooling. Note that the spatial compositional fluctuations of amplitude are larger for **sample 1** (ranging $2.0 \times 10^{19} \text{ cm}^{-3}$) than for **sample 4** (ranging $5.0 \times 10^{20} \text{ cm}^{-3}$) calculated by difference in composition, which coincides with the observed trends in thermal conductivity where **sample 4** has the lowest thermal conductivity. Based on these chemical maps, we suggest that there are presumably distinct nanoscale regions in CZTS where this material is at least partially disordered. This suggestion is supported by compositional inhomogenities at nanoscale from entropy-driven cation clustering expected from the motif-based model⁴⁴. However, the origin of this behavior still remains unclear. Even so, we believe that cation fluctuation is influenced by the native phase space in which CZTS can form S-Cu₃Sn and S-CuSnZn₂ motifs⁴⁴.

Enhancement of electrical and TE properties

Admittance spectroscopy (AS) measurements were used to characterize the defect levels and concentrations in samples. Figure 5a shows an Arrhenius plot to verify the defect levels, which were extracted from inflection points from the AS curves in Figs. 5b-d. All parameters for AS measurement are shown in Supplementary Table 3. The activation energy, $E(\omega)$, were obtained from the slope of the Arrhenius plot, $\ln(\omega_0/T^2)$ versus $1/T$, where ω_0 is the inflection point of the capacitance versus frequency. The shallow acceptor level becomes lower in the Cu-poor composition from 100 meV to 65 meV because the dominant acceptor is V_{Cu} . The Na-doping in Cu-deficient compositions results in two orders of magnitude higher hole concentration compared to stoichiometric compositions because there is a reduction in the degree of compensation²⁹. The

dual advantages of lower thermal activation energy and higher hole concentration dramatically improve electrical properties by tuning composition and doping.

The Seebeck coefficient of CZTS single crystal along a -axis is large, for example as Na: 0.1 mol% **sample 3**, $290 \mu\text{V/K}$ at 300 K and $347 \mu\text{V/K}$ at 800 K. As mentioned above, we suggested that it is possible to tune DOS by the formation of V_{Cu} in Cu-deficient samples and Na-doping. The energetic defect DOS is obtained by converting frequency into energy by using equations (1) and (2)⁴⁵.

$$E(\omega) = k_{\text{B}}T \cdot \ln\left(\frac{2\xi T^2}{\omega}\right) \quad (1)$$

$$N_{\text{t}}(E(\omega)) = -\frac{V_{\text{bi}}}{W_{\text{d}}} \cdot \frac{dC}{d\omega} \cdot \frac{\omega}{k_{\text{B}}T} \quad (2)$$

Where N_{t} is integrated defect density, ζ is pre-exponential factor comprising all temperature independent terms, V_{bi} is built-in potential, W_{d} is depletion width. V_{bi} and W_{d} are extracted from capacitance-voltage measurement. Figure 5e reveals DOS of dominant acceptor levels extracted from AS data. The enhancement of DOS with shallow acceptor and Na-doping relating to TE properties can be observed. Considering the impact of Na on DOS in CZTS, perhaps low compensation, we present the DOS for the Na-dopant substitution on Cu by DFT calculation in Supplementary Fig. 7. There are no significant increase in DOS by Na_{Cu} defect, on the other hand the effective masses for each valence band are slightly larger than stoichiometric CZTS. Other possible Na impact on DOS is the increasing of Na substitution on Zn site (Na_{Zn}) shallow acceptor defect which is low formation energy next to Na_{Cu} ³¹. We experimentally demonstrate that DOS in CZTS can be improved by Cu-deficit and Na-doping for high TE performance.

Conclusions

In this study, our focus was to first achieve competitive ZT values for kesterite CZTS as totally environmentally friendly TE material by novel pseudo-cubic approach based on valleytronics. The value of $ZT = 1.6$ at 800 K in high-quality p-type CZTS single crystals is remarkable and due primarily to high degeneracy at valence band edge (valley degeneracy), the anisotropy of effective mass (valley anisotropy) and localized lattice distortion. Several insights (a)-(c) for a high ZT quaternary compound can be highlighted from this study as follows: (a) high PF value 1.9×10^{-3} W/mK² at 800 K was obtained by tuning valley parameters, (b) the intrinsic local cation anti-site disorder and cation fluctuation results in a low thermal conductivity of ~ 0.94 W/mK at 800 K even for single crystal samples, (c) Cu-deficient composition and Na-doping lead to high electrical and TE properties due to V_{Cu} and Na related shallow acceptor defects. Compared to other high performance TE materials, our results for CZTS demonstrate that a high ZT can be realized in an intrinsic structure, as single crystal, with simple tuning by composition and doping without complex nanostructuring. This is the evidence that valleytronics have a potential to produce intrinsic TE material compared with state-of-the-art concepts. We expect the discovery of high TE performance for CZTS could attract great attention within the waste heat recovery industry due to the totally environmentally friendly combination of elements that are low cost, non-toxic, and earth-abundant.

Methods

Single crystal growth. CZTS single crystals were grown by Sn-solvent traveling heater method (THM) at 40 °C/cm axial temperature gradient, a growth temperature at 850 °C, at a growth speed of 4 mm/day. The details are explained in Supplementary Information. A conical quartz ampoule

was coated with carbon to avoid solution adhesion. The detailed composition of the crystals was determined by inductively coupled plasma atomic emission spectroscopy (ICP-AES; SII NanoTechnology SPS3520UV). Samples were dissolved into a mixed acid containing HNO₃ and HCl.

Sample preparation before characterization. Grown crystals were cut with a diamond blade and polished mechanically with 0.01 μm Al₂O₃ powder and then etched with a HCl solution for 5 minutes to remove saw and polishing damage. The electrical and TE measurements were carried out along the *c*-axis in Supplementary Fig. 1c.

DFT calculation. First-principle calculations were performed using the plane-wave basis projector augmented wave (PAW)⁴⁶ method and the generalized gradient approximation (GGA) of Perdew-Burke-Ernzerhof (PBE)⁴⁷ implemented in Vienna *Ab initio* Simulation Package (VASP)^{48, 49}. The planewave basis-set cutoff was set to 300 eV and spin polarization was considered. We used the PAW potentials which treat Cu (3d¹⁰ 4s¹), Zn (3d¹⁰ 4s²), Sn (4d¹⁰ 5s² 5p²), S (3s² 3p⁴), and Na (2p⁶ 3s¹) explicitly as valence electrons and the rest as core electrons. We adopted the effective Hubbard *U* values of 5.2 eV for Cu, 6.5 eV for Zn, and 3.5 eV for Sn. Atomic positions and the unit cell parameters were relaxed until the forces on all atoms become less than 2.0×10⁻² eV/Å. A Na-doped model with the concentration of 6.25% was constructed by substituting a Na atom for a Cu site within a 2×2×1 supercell of the conventional unit cell. The substitution for Cu 2a site was considered because the energy was lower than that for Cu 2c site. The Brillouin zones were sampled with 4×4×2 and 2×2×2 Monkhorst–Pack k-point meshes for the unit cell and 2×2×1 supercell, respectively. For electronic DOS, the 2×2×1 supercell and finer Γ -centered k-point mesh of 4×4×4 were used for both pristine and Na-doped CZTS models. For electronic band structure, a conventional unit cell instead of a primitive cell was intentionally used

for the ease of analyzing anisotropic effective masses along the a and c directions. The band unfolding for the Na-doped supercell were performed using Band UP code⁵⁰.

Characterization. The structural properties were analyzed by powder X-ray diffraction (XRD; Panalytical X' Pert PRO) and Raman spectroscopy (HORIBA T64000). XRD measurement was operated under 40 kV and 40 mA using a Cu-K α radiation source. A 514 nm Ar⁺ laser was used in the Raman measurements and focused on the sample by an objective lens with a numerical aperture of 0.55. The laser power on the sample was 100 mW. The spectra were calibrated based on 520 cm⁻¹ of Si peak.

The disorder structure in stoichiometric CZTS single crystal was performed by STEM (JEOL 2800) operated at 200 kV using two simultaneous solid-state EDX detectors. The spectral image acquisition was performed over a series of consecutive sub-second frames with drift correction between frames with a total acquisition time of less than 20 min. The EDX data were processed using Thermo-Scientific Image Analysis software. The X-ray emission spectra captured were quantified after subtracting the background and each of elements. The analytical certainty associated with EDX profiling is within 0.5 at.%.

The electrical conductivity σ and Seebeck coefficient S were measured simultaneously in a helium atmosphere at 300-800 K using a commercial system (ZEM3; ADVANCE RIKO) on the samples with the dimension of about 2 mm \times 2 mm \times 10 mm. Thermal conductivity κ was calculated based on the equation: $\kappa = \lambda C_p D$, where λ is the thermal diffusivity, C_p is the specific heat capacity, and D is the density. The thermal diffusivity was measured by laser flash method (Netzsch; LFA457) on the rectangular samples with 8 mm \times 8 mm \times 1 mm coated with a thin layer of graphite to minimize errors from the emissivity of the material. The specific heat capacity was measured by differential scanning calorimetry (DSC; Rigaku Thermo plus EVO2 DSCvesta) on

the samples with 3 mm×3 mm×3 mm. The mass of all samples is unchanged after measurements by using Thermogravimetric analysis (TGA) in Supplementary Fig. 7. The density values between 4.4-4.5 g/cm³ were measured using the Archimedes method at room temperature.

The hole concentration p and mobility μ were measured by temperature dependence of Hall effect (TOYO; ResiTest8300) performed in a 0.45 T magnetic field in the van der Pauw geometry under a helium atmosphere at 20-800 K. For Hall measurements, Au contacts, each with a diameter of 1 mm and thickness of 200-300 nm, were evaporated onto the corners of each CZTS bulk single crystal with the dimension of 5 mm×5 mm×0.8 mm.

Admittance spectroscopy measurements were carried out in the temperature of 120-300 K under dark condition with a LCR meter (HP 4284A), which applied an AC voltage of 50 mV by varying the frequencies from 100 Hz to 1 MHz. Schottky diode structures of 1 mm diameter Al Schottky contact/CZTS (5 mm×5 mm×1 mm)/Au Ohmic back contact were fabricated by evaporation. The thickness of contacts was 300-400 nm.

Data availability

The data that support the findings of this study are available from the authors on reasonable request.

References

1. Slack, G. A. in *CRC Handbook of Thermoelectricity*, (CRC Press, 1995), pp. 407–440.
2. Liu, H. *et al.* Copper ion liquid-like thermoelectrics. *Nat. Mater.* **11**, 422–425 (2012).
3. Olvera, A. A. *et al.* Partial indium solubility induces chemical stability and colossal thermoelectric figure of merit in Cu₂Se. *Energy Environ. Sci.* **10**, 1668–1676 (2017).

4. Ibáñez, M. *et al.* High-performance thermoelectric nanocomposites from nanocrystal building blocks. *Nat. Commun.* **7**, 10766 (2016).
5. Zhang, J. *et al.* Discovery of high-performance low-cost n-type Mg_3Sb_2 -based thermoelectric materials with multi-valley conduction bands. *Nat. Commun.* **8**, 13901 (2017).
6. Luo, Y. *et al.* Progressive Regulation of Electrical and Thermal Transport Properties to High-Performance CuInTe_2 Thermoelectric Materials. *Adv. Energy Mater.* **6**, 1600007 (2016).
7. Fu, C. *et al.* Realizing high figure of merit in heavy-band *p*-type half-Heusler thermoelectric materials. *Nat. Commun.* **6**, 8144 (2015).
8. Cheng, Y. *et al.* New insight into InSb -based thermoelectric materials from a divorced eutectic design to a remarkably high thermoelectric performance. *J. Mater. Chem. A Mater.* **5**, 5163–5170 (2017).
9. Heremans, J. P. *et al.* Enhancement of Thermoelectric Efficiency in PbTe by Distortion of the Electronic Density of States. *Science* **321**, 554–557 (2008).
10. Wang, H., Gibbs, Z. M., Takagiwa, Y. & Snyder, G. J. Tuning bands of PbSe for better thermoelectric efficiency. *Energy Environ. Sci.* **7**, 804–811 (2014).
11. Hicks, L. D. & Dresselhaus, M. S. Effect of quantum-well structures on the thermoelectric figure of merit. *Phys. Rev. B* **47**, 12727–12731 (1993).
12. Heremans, J. P., Thrush, C. M. & Morelli, D. T. Thermopower enhancement in lead telluride nanostructures. *Phys. Rev. B* **70**, 115334 (2004).
13. Hsu, K. F. *et al.* Cubic AgPbmSbTe_{2+m} : Bulk Thermoelectric Materials with High Figure of Merit. *Science* **303**, 818–821 (2004).
14. Biswas, K. *et al.* Strained endotaxial nanostructures with high thermoelectric figure of merit. *Nat. Chem.* **3**, 160–166 (2011).

15. Biswas, K. *et al.* High-performance bulk thermoelectrics with all-scale hierarchical architectures. *Nature* **489**, 414–418 (2012).
16. Su, X. *et al.* Multi-Scale Microstructural Thermoelectric Materials: Transport Behavior, Non-Equilibrium Preparation, and Application. *Adv. Mater.* **29**, 1602013 (2017).
17. Zhao, L. D. *et al.* Ultralow thermal conductivity and high thermoelectric figure of merit in SnSe crystals. *Nature* **508**, 373–377 (2014).
18. Li, C. W. *et al.* Orbitally driven giant phonon anharmonicity in SnSe. *Nat. Phys.* **11**, 1063–1069 (2015).
19. Duong, A. T. *et al.*, Achieving $ZT = 2.2$ with Bi-doped n-type SnSe single crystals. *Nat. Commun.* **7**, 13713 (2016).
20. Zhao, L. D. *et al.* Ultrahigh power factor and thermoelectric performance in hole-doped single-crystal SnSe. *Science* **351**, 141–144 (2016).
21. Peng, K. *et al.* Broad temperature plateau for high ZT s in heavily doped p-type SnSe single crystals. *Energy Environ. Sci.* **9**, 454–460 (2016).
22. Chang, C. *et al.* 3D charge and 2D phonon transports leading to high out-of-plane ZT in n-type SnSe crystals. *Science* **360**, 778–783 (2018).
23. Wu, H. *et al.* Sodium-Doped Tin Sulfide Single Crystal: A Nontoxic Earth-Abundant Material with High Thermoelectric Performance. *Adv. Energy Mater.* **8**, 1800087 (2018).
24. Schaibley, J. R. *et al.* Valleytronics in 2D materials. *Nat. Rev. Mater.* **1**, 16055 (2016).
25. Zhang, J. *et al.*, High-Performance Pseudocubic Thermoelectric Materials from Non-cubic Chalcopyrite Compounds. *Adv. Mater.* **26**, 3848–3853 (2014).
26. Nagaoka, A., Yoshino, K., Taniguchi, H., Taniyama, T. & Miyake, H. Preparation of $\text{Cu}_2\text{ZnSnS}_4$ single crystals from Sn solutions. *J. Crystal Growth* **341**, 38–41 (2012).

27. Nagaoka, A., Masuda, T., Yasui, S., Taniyama, T. & Nose, Y. The single-crystal multinary compound $\text{Cu}_2\text{ZnSnS}_4$ as an environmentally friendly high-performance thermoelectric material. *Appl. Phys. Express* **11**, 051203 (2018).
28. Phuong, L. Q. *et al.*, Free-carrier dynamics and band tails in $\text{Cu}_2\text{ZnSn}(\text{S}_x\text{Se}_{1-x})_4$: Evaluation of factors determining solar cell efficiency. *Phys. Rev. B* **92**, 115204 (2015).
29. Nagaoka, A. *et al.* Effects of sodium on electrical properties in $\text{Cu}_2\text{ZnSnS}_4$ single crystal. *Appl. Phys. Lett.* **104**, 152101 (2014).
30. Chen, S., Yang, J. H., Gong, X. G., Walsh, A. & Wei, S. H. Intrinsic point defects and complexes in the quaternary kesterite semiconductor $\text{Cu}_2\text{ZnSnS}_4$. *Phys. Rev. B* **81**, 245204 (2010).
31. Xiao, W. *et al.* Intrinsic defects and Na doping in $\text{Cu}_2\text{ZnSnS}_4$: A density-functional theory study. *Solar Energy* **116**, 125 (2015).
32. Liu, M. L., Huang, F. Q., Chen, L. D. & Chen, I. W. A wide-band-gap *p*-type thermoelectric material based on quaternary chalcogenides of $\text{Cu}_2\text{ZnSnQ}_4$ ($Q=\text{S}, \text{Se}$). *Appl. Phys. Lett.* **94**, 202103 (2009).
33. Yang, H., Jauregui, L. A., Zhang, G., Chen, Y. P. & Wu, Y. Nontoxic and Abundant Copper Zinc Tin Sulfide Nanocrystals for Potential High-Temperature Thermoelectric Energy Harvesting. *Nano Lett.* **12**, 540-545 (2012).
34. Kosuga, A., Matsuzawa, M., Horie, A., Omoto, T. & Funahashi, R. High-temperature thermoelectric properties and thermal stability in air of copper zinc tin sulfide for the *p*-type leg of thermoelectric devices. *Jpn. J. Appl. Phys.* **54**, 061801 (2015).

35. Gürel, T., Sevik, C. & Çağın, T. Characterization of vibrational and mechanical properties of quaternary compounds $\text{Cu}_2\text{ZnSnS}_4$ and $\text{Cu}_2\text{ZnSnSe}_4$ in kesterite and stannite structures. *Phys. Rev. B* **84**, 205201 (2011).
36. Clarke, D. R. & Phillpot, S. R. Thermal barrier coating materials. *materialstoday* **8**, 22-29 (2005).
37. Sparks, T. D., Fuierer, P. A. & Clarke, D. R. Anisotropic Thermal Diffusivity and Conductivity of La-Doped Strontium Niobate $\text{Sr}_2\text{Nb}_2\text{O}_7$. *J. Am. Ceram. Soc.* **93**, 1136-1141 (2010).
38. Qu, Z., Sparks, T. D., Pan, W. & Clarke, D. R. Thermal conductivity of the gadolinium calcium silicate apatites: Effect of different point defect types. *Acta Materialia* **59**, 3841-3850 (2011).
39. Shi, X. Y., Huang, F. Q., Liu, M. L. & Chen, L. D. Thermoelectric properties of tetrahedrally bonded wide-gap stannite compounds $\text{Cu}_2\text{ZnSn}_{1-x}\text{In}_x\text{Se}_4$. *Appl. Phys. Lett.* **94**, 122103 (2009).
40. Ibáñez, M. *et al.* Composition Control and Thermoelectric Properties of Quaternary Chalcogenide Nanocrystals: The Case of Stannite $\text{Cu}_2\text{CdSnSe}_4$. *Chem. Mater.* **24**, 562-570 (2012).
41. Kosyak, V., Karmakar, M. A. & Scarpulla, M. A. Temperature dependence conductivity of polycrystalline $\text{Cu}_2\text{ZnSnS}_4$ thin films. *Appl. Phys. Lett.* **100**, 263903 (2012).
42. Gaultois, M. W. & Sparks, T. D. How much improvement in thermoelectric performance can come from reducing thermal conductivity?. *Appl. Phys. Lett.* **104**, 113906 (2014).
43. He, Y. *et al.* High thermoelectric performance in non-toxic earth-abundant copper sulfide. *Adv. Mater.* **26**, 3974–3978 (2014).

44. Zawadzki, P., Zakutayev, A. & Lany, S. Entropy-Driven Clustering in Tetrahedrally Bonded Multinary Materials. *Phys. Rev. Appl.* **3**, 034007 (2015).
45. Walter, T., Herberholz, R., Müller, C. & Schock, H. W. Determination of defect distributions from admittance measurements and application to Cu(In, Ga)Se₂ based heterojunctions. *J. Appl. Phys.* **80**, 4411-4420 (1996).
46. Blöchl, P. E. Projector augmented-wave method. *Phys. Rev. B* **50**, 17953-17979 (1994).
47. Perdew, J. P., Burke, K. & Ernzerhof, M. Generalized gradient approximation made simple. *Phys. Rev. Lett.* **77**, 3865-3868 (1996).
48. Kresse, G. & Hafner, J. *Ab initio* molecular dynamics for liquid metals. *Phys. Rev. B* **47**, 558–561 (1993).
49. Kresse, G. & Furthmüller, J. *Phys. Rev. B* **54**, 11169–11186 (1996).
50. Medeiros, P. V. C., Stafström, S. & Björk, J. Effects of extrinsic and intrinsic perturbations on the electronic structure of graphene: Retaining an effective primitive cell band structure by band unfolding. *Phys. Rev. B* **89**, 041407(R) (2014)

Acknowledgements

A.N. acknowledges supports from the JSPS for a Research Fellow Grant-in-Aid and the scholarship of Smart Grid Home Co., Ltd. T.D.S. acknowledges support from National Science Foundation CAREER award 1651668.

Author contributions

A.N. and K.N. designed, conducted the all experiments and prepared the manuscript. K.Y. and M.A.S helped in single crystal growth and electrical measurements. T.M. conducted theoretical

calculation. T.D.S. helped in thermoelectric measurements. All authors contributed to the discussion of results and approved the final version of the manuscript.

Additional information

Supplementary Information accompanies this paper at

Competing financial interests: The authors declare no competing financial interests.

Figures

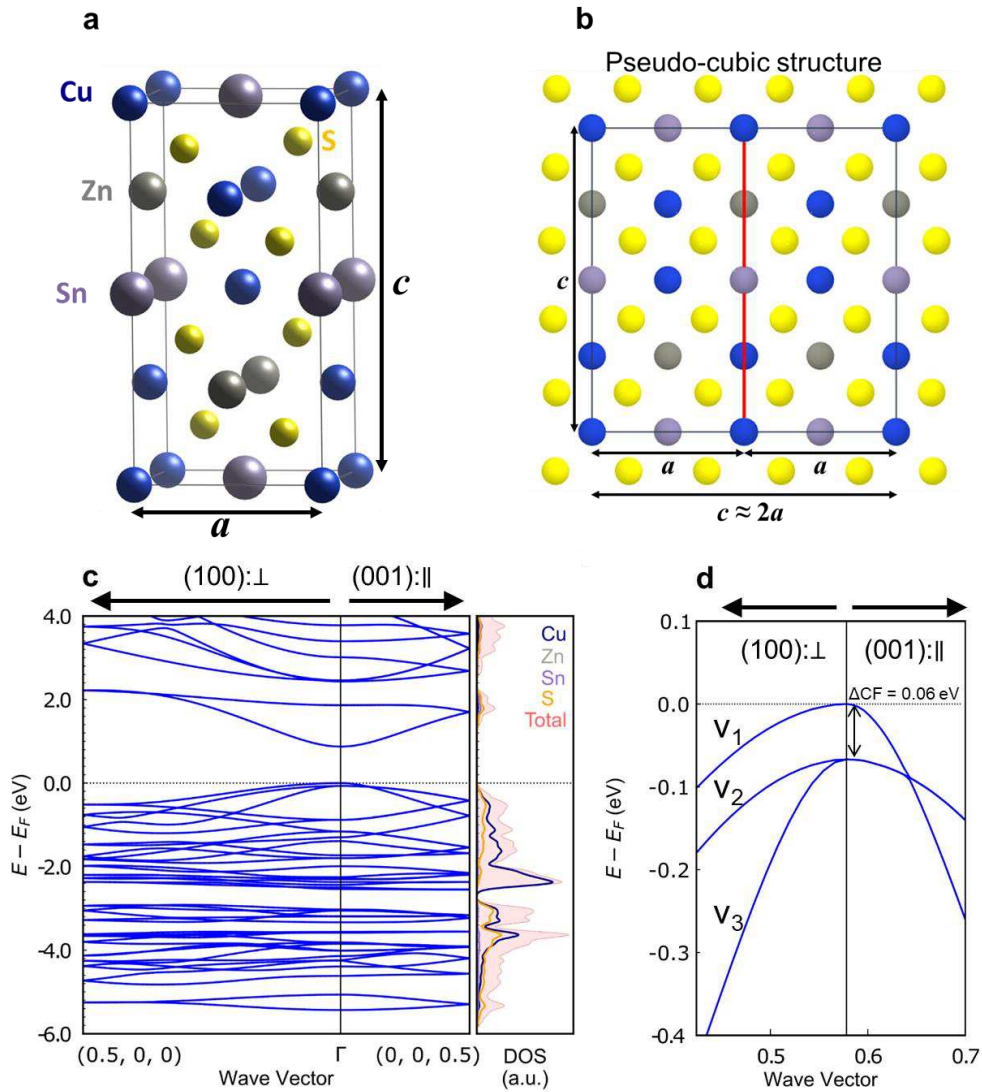


Figure 1 Pseudo-cubic approach based on valleytronics in TE CZTS material. a, Conventional unit cell of the kesterite structure having **b,** pseudo-cubic structure by the crystal structure parameter η ($c/2a$) ≈ 1 . **c,** Electronic band structure of kesterite structure of CZTS along the two symmetry directions (100) and (001). **d,** The top of the valence band is split into the topmost (v_1) and second (v_2) bands with Γ_{7+8} symmetry and the third band (v_3) with Γ_{5+6} symmetry where the single state is above the twofold degenerate state with the energy splitting parameter $\Delta CF = 0.06$ eV in the vicinity of Γ point. Dashed line denote the Fermi energy.

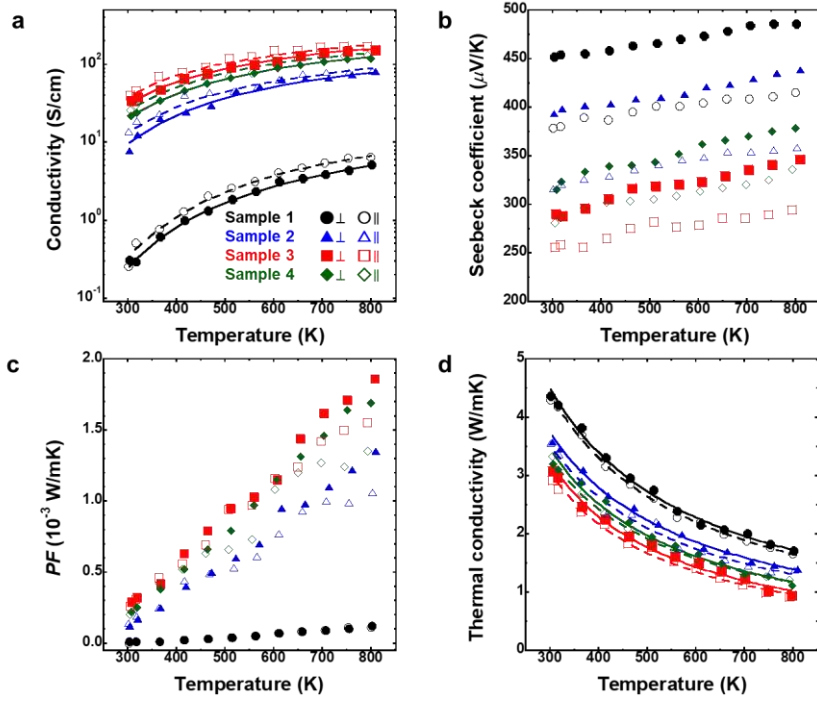


Figure 2 TE characterization of CZTS single crystals. Temperature dependence of **a**, electrical conductivity σ fitted by $\sigma(T) = \sigma_B \exp(-E_A/k_b T)$; **b**, Seebeck coefficient S ; **c**, power factor PF ; and **d**, thermal conductivity κ . Lines are roughly following to a T^{-1} relation. Measurements are carried out in the transverse (\perp ; perpendicular to the c -axis) and the longitudinal (\parallel ; parallel to the c -axis) directions.

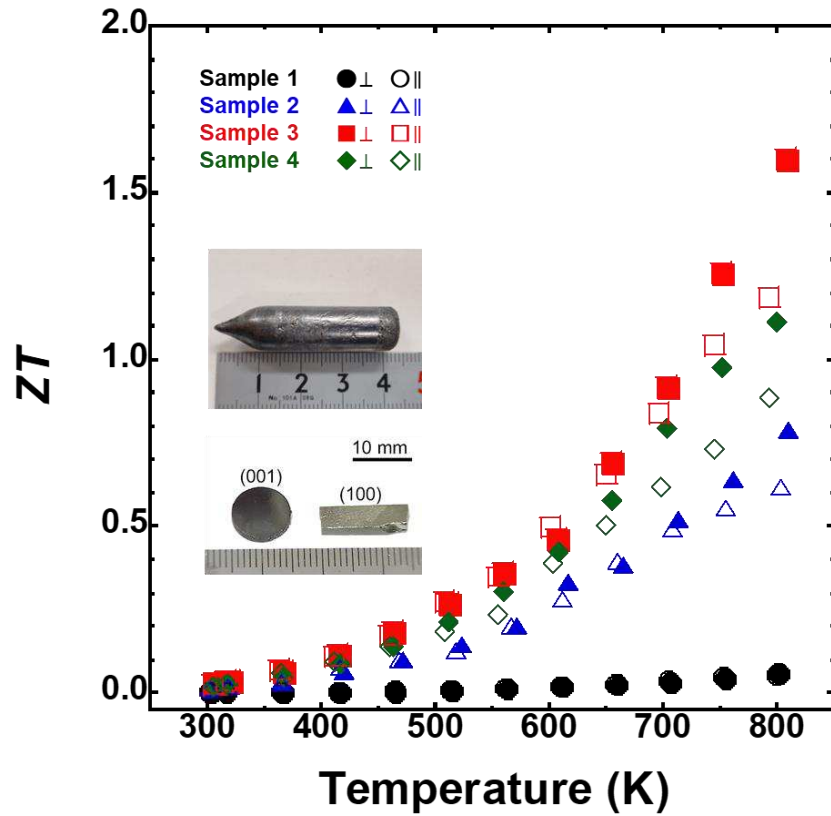


Figure 3 Temperature dependence of the dimensionless figure of merit ZT for different compositional CZTS single crystals. The insets are a typical CZTS ingot and samples cutting along the (100) and (001) planes.

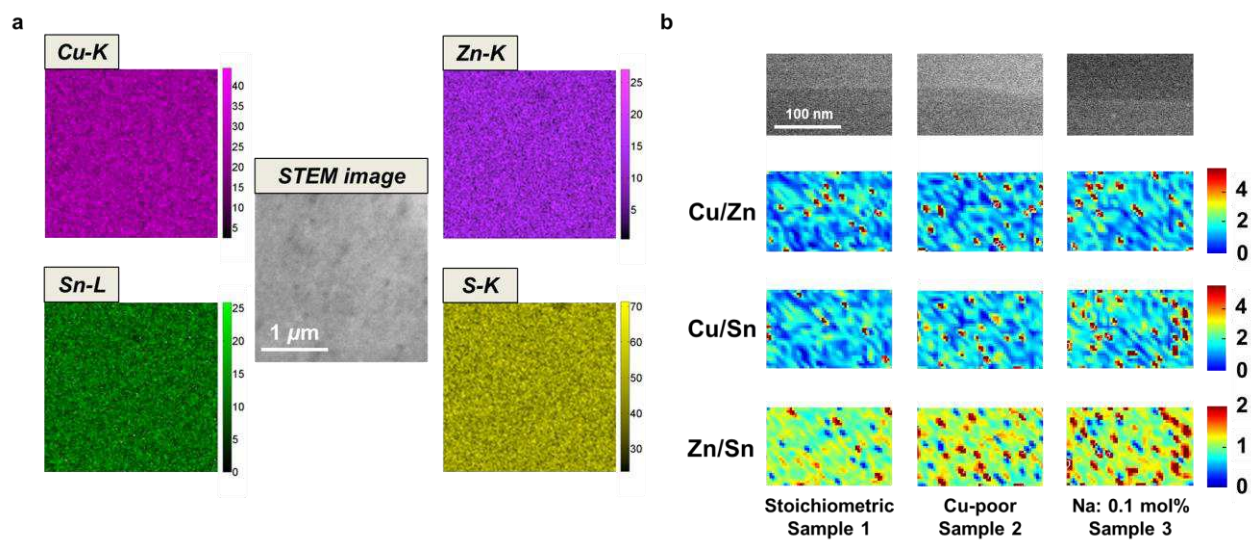


Figure 4 The cation fluctuation by high-resolution STEM image. **a**, STEM-based EDX mapping images of stoichiometric **sample 1** at micrometer scale. Stoichiometric Cu:Zn:Sn:S = 24.6:13.0:12.2:50.2 could be observed, and there is local compositional non-uniformity in large scale. **b**, Elemental correlations for Cu/Zn, Cu/Sn, and Zn/Sn at nanometer scale. Considering stoichiometric ratio of Cu/Zn = 2, Cu/Sn = 2, and Zn/Sn = 1, the large cation fluctuation with spatial compositional amplitude less than 0.5 at.% could be observed in **samples 1-3** at high magnification.

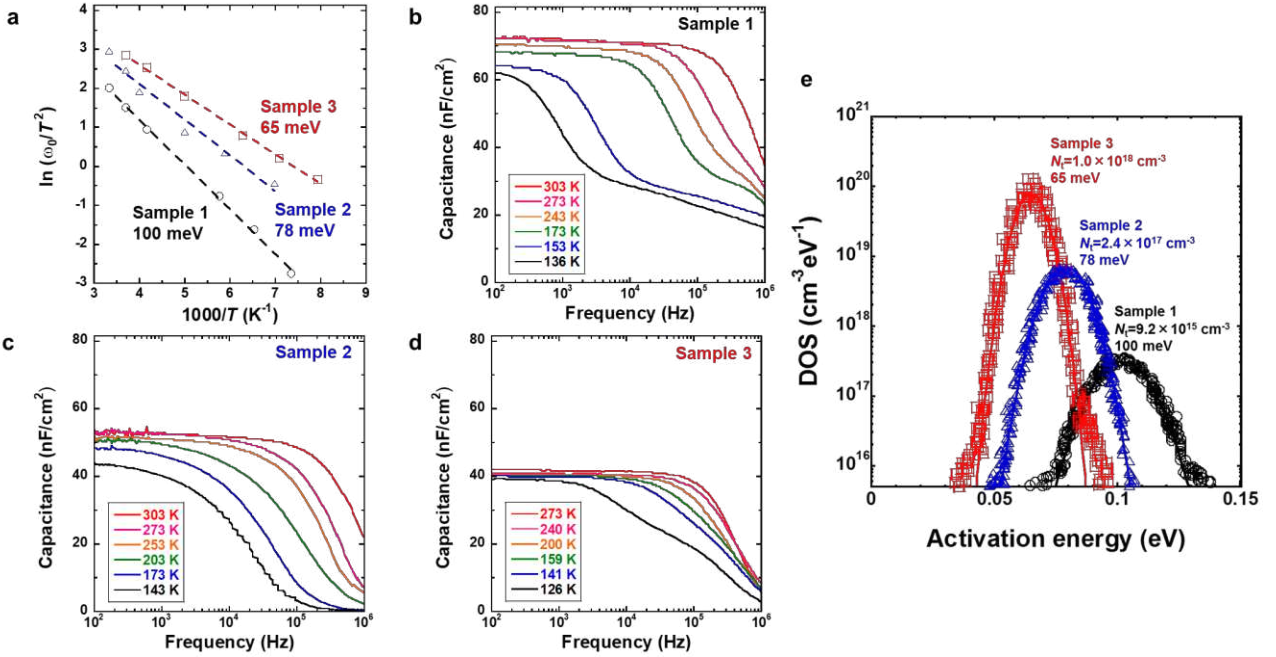


Figure 5 The defect level and DOS of CZTS single crystals extracted by AS measurement as a function of temperature. **a**, Arrhenius plot of ω_0/T^2 , ω_0 being the angular emission frequency of the inflection points. **b-d**, Temperature dependence of AS spectra of each sample. **e**, N_t calculated from AS measurement for different compositional samples. The defect level and DOS values are shallower and higher with Cu-poor and Na-doping, respectively. Associated integrated N_t is calculated based on Gaussian fitting. No anisotropy of defect properties can be observed.

Table 1 Anisotropy of the effective hole masses (m_n for $n = v_1, v_2,$ and v_3 in Fig. 1) in CZTS. m_e is electron mass. The transverse \perp masses are determined from the energy dispersions in (100) direction, and the longitudinal \parallel masses are determined from the dispertions in (001) direction.

$m_{v_1}^{\perp} [m_e]$	$m_{v_1}^{\parallel} [m_e]$	$m_{v_2}^{\perp} [m_e]$	$m_{v_2}^{\parallel} [m_e]$	$m_{v_3}^{\perp} [m_e]$	$m_{v_3}^{\parallel} [m_e]$
0.77	0.17	0.78	0.76	0.16	0.76

Figures

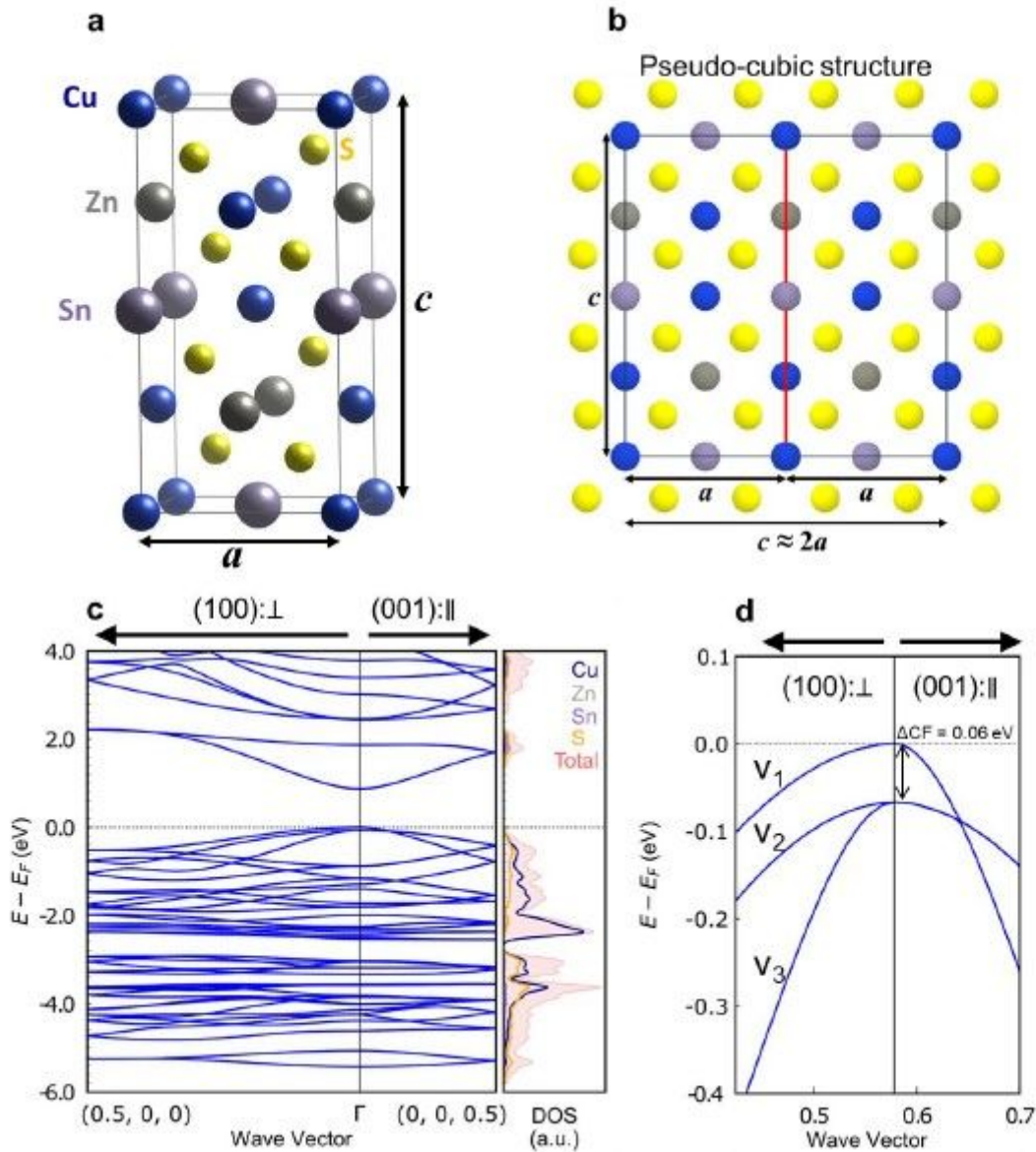


Figure 1

Pseudo-cubic approach based on valleytronics in TE CZTS material. a, Conventional unit cell of the kesterite structure having b, pseudo-cubic structure by the crystal structure parameter η ($c/2a$) ≈ 1 . c, Electronic band structure of kesterite structure of CZTS along the two symmetry directions (100) and (001). d, The top of the valence band is split into the topmost (v_1) and second (v_2) bands with $\Gamma 7+8$ symmetry and the third band (v_3) with $\Gamma 5+6$ symmetry where the single state is above the twofold degenerate state with the energy splitting parameter $\Delta CF = 0.06$ eV in the vicinity of Γ point. Dashed line denote the Fermi energy.

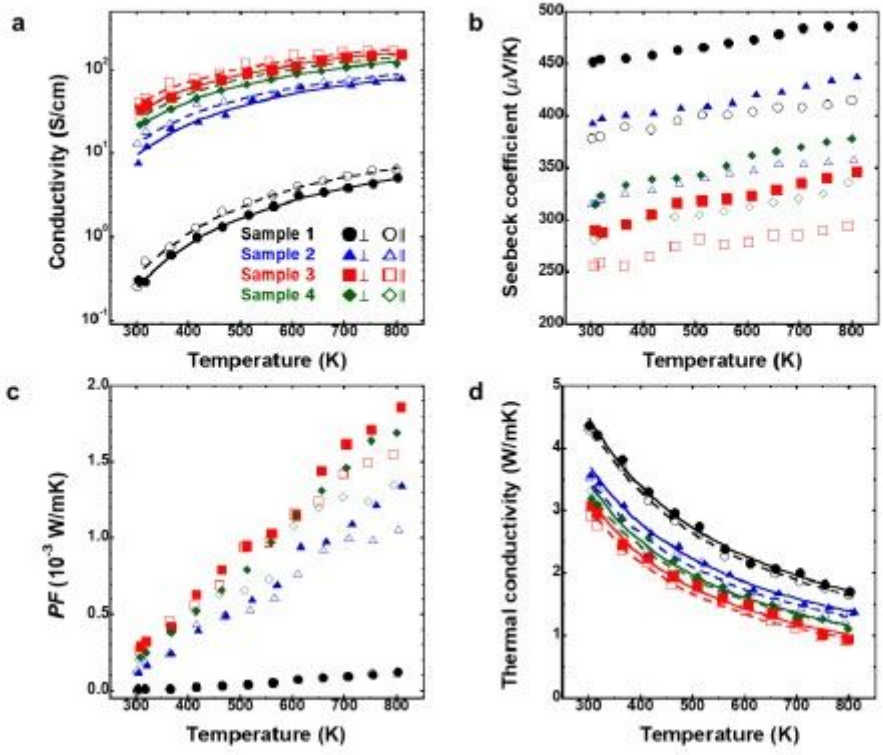


Figure 2

TE characterization of CZTS single crystals. Temperature dependence of a, electrical conductivity σ fitted by $\sigma(T) = \sigma_0 \exp(-A/bT)$; b, Seebeck coefficient S ; c, power factor PF; and d, thermal conductivity κ . Lines are roughly following to a T^{-1} relation. Measurements are carried out in the transverse (\perp ; perpendicular to the c-axis) and the longitudinal (\parallel ; parallel to the c-axis) directions.

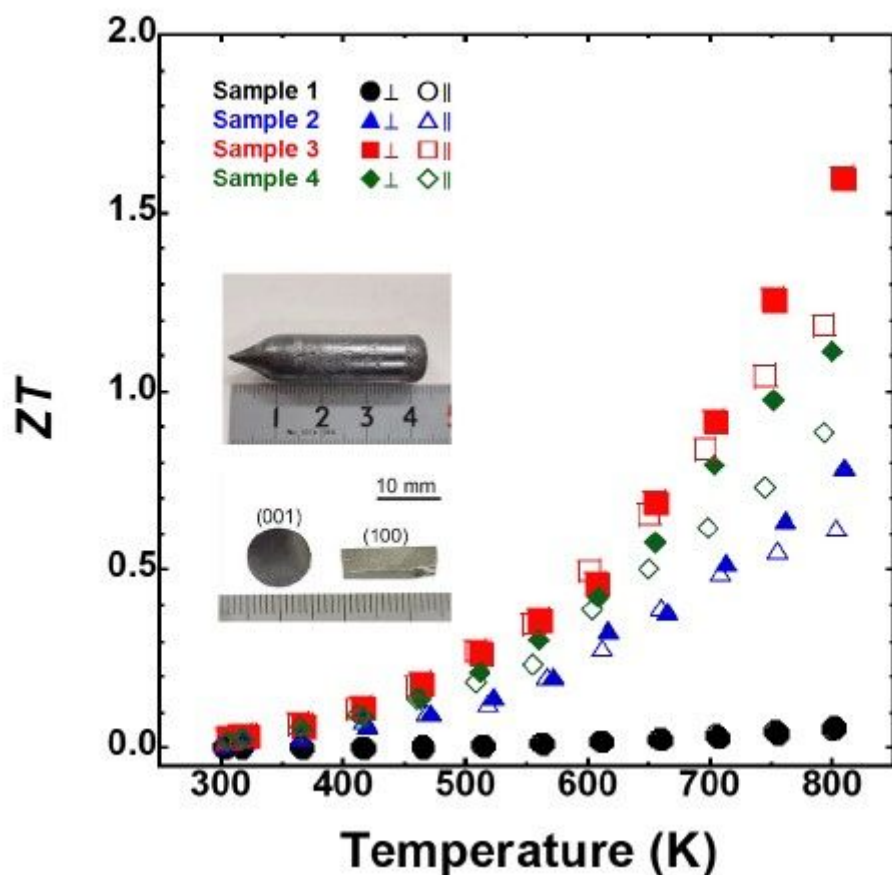


Figure 3

Temperature dependence of the dimensionless figure of merit ZT for different compositional CZTS single crystals. The insets are a typical CZTS ingot and samples cutting along the (100) and (001) planes.

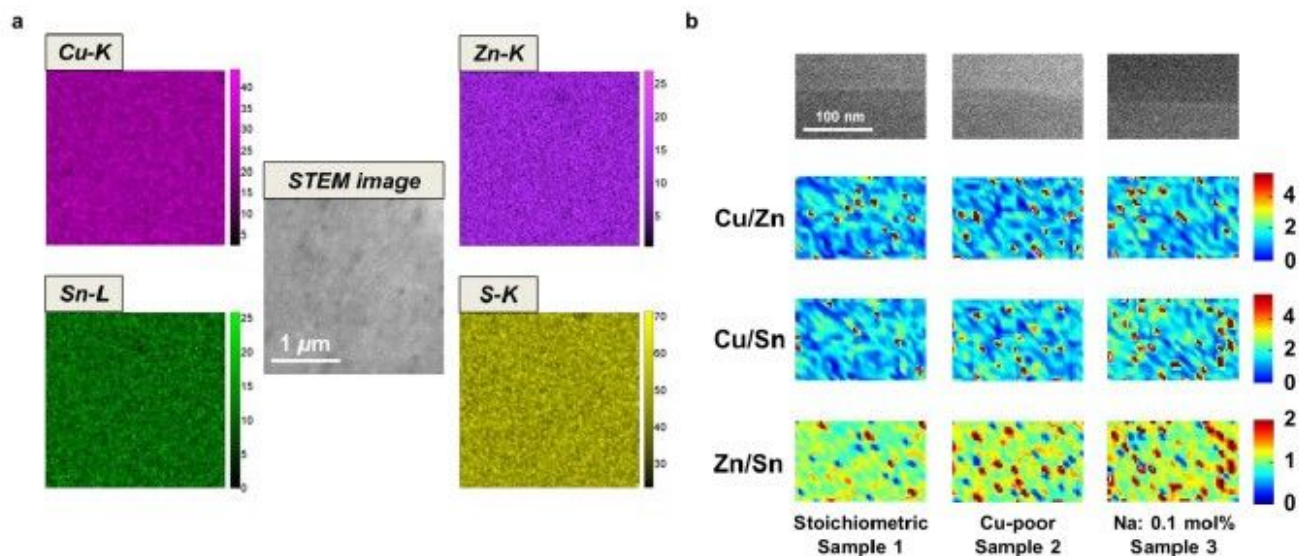


Figure 4

The cation fluctuation by high-resolution STEM image. a, STEM-based EDX mapping images of stoichiometric sample 1 at micrometer scale. Stoichiometric Cu:Zn:Sn:S = 24.6:13.0:12.2:50.2 could be observed, and there is local compositional non-uniformity in large scale. b, Elemental correlations for Cu/Zn, Cu/Sn, and Zn/Sn at nanometer scale. Considering stoichiometric ratio of Cu/Zn = 2, Cu/Sn = 2, and Zn/Sn = 1, the large cation fluctuation with spatial compositional amplitude less than 0.5 at.% could be observed in samples 1-3 at high magnification.

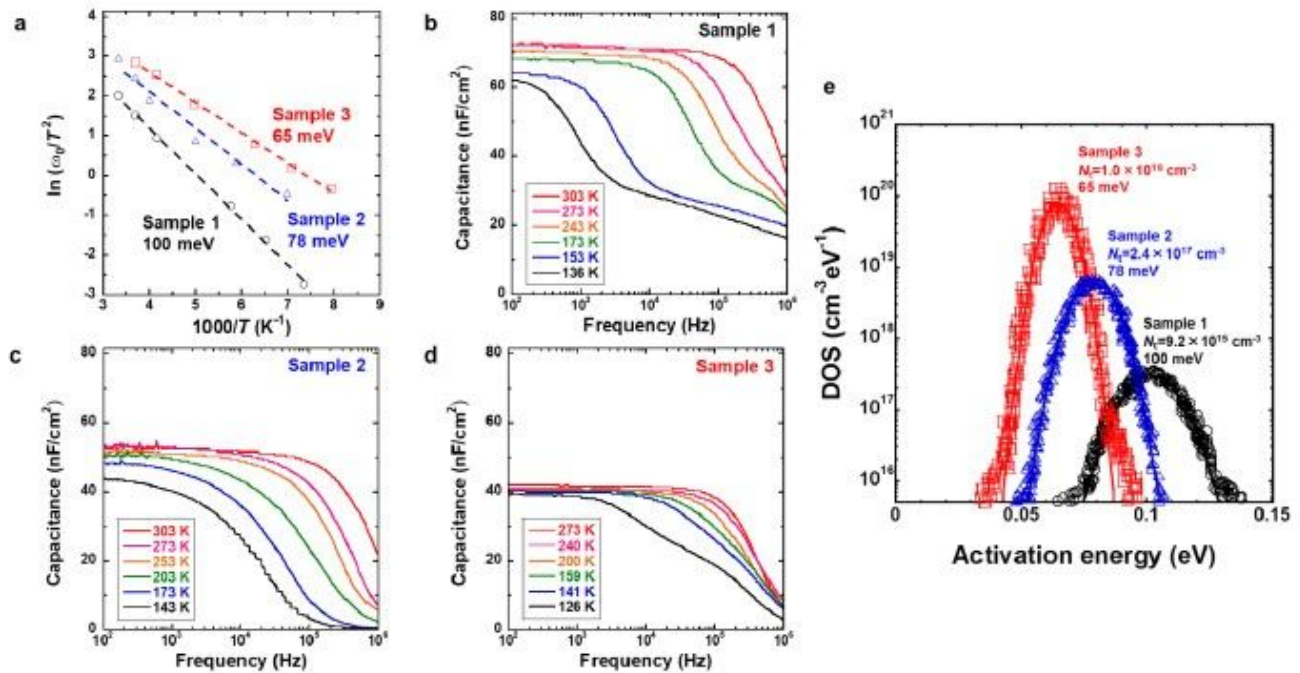


Figure 5

The defect level and DOS of CZTS single crystals extracted by AS measurement as a function of temperature. a, Arrhenius plot of ω_0/T^2 , ω_0 being the angular emission frequency of the inflection points. b-d, Temperature dependence of AS spectra of each sample. e, N_t calculated from AS measurement for different compositional samples. The defect level and DOS values are shallower and higher with Cu-poor and Na-doping, respectively. Associated integrated N_t is calculated based on Gaussian fitting. No anisotropy of defect properties can be observed.

Supplementary Files

This is a list of supplementary files associated with this preprint. Click to download.

- [SupplementaryinformationTECZTS.pdf](#)
- [FigureS1.jpg](#)
- [FigureS2.jpg](#)
- [FigureS3.jpg](#)
- [FigureS4.jpg](#)

- FigureS5.jpg
- FigureS6.jpg
- FigureS7.jpg
- FigureS8.jpg
- TableS1.png
- TableS2.png
- TableS3.png
- TableS4.png
- TableS5.png
- TableS6.png